S100A4 regulates macrophage invasion by distinct myosin-dependent and myosin-independent mechanisms

Natalya G. Dulyaninova[a], Penelope D. Ruiz[b], Matthew J. Gamble[b], Jonathan M. Backer[a,b,*], and Anne R. Bresnick[a,*]
[a]Department of Biochemistry and [b]Department of Molecular Pharmacology, Albert Einstein College of Medicine, Bronx, NY 10461

ABSTRACT S100A4, a member of the S100 family of Ca^{2+}-binding proteins, is a key regulator of cell migration and invasion. Our previous studies showed that bone marrow–derived macrophages from S100A4$^{-/-}$ mice exhibit defects in directional motility and chemotaxis in vitro and reduced recruitment to sites of inflammation in vivo. We now show that the loss of S100A4 produces two mechanistically distinct phenotypes with regard to macrophage invasion: a defect in matrix degradation, due to a disruption of podosome rosettes caused by myosin-IIA overassembly, and a myosin-independent increase in microtubule acetylation, which increases podosome rosette stability and is sufficient to inhibit macrophage invasion. Our studies point to S100A4 as a critical regulator of matrix degradation, whose actions converge on the dynamics and degradative functions of podosome rosettes.

INTRODUCTION

S100A4 is a member of the S100 family of Ca^{2+}-binding proteins. The S100 proteins, which are found exclusively in vertebrates, are typically symmetric homodimers. Each subunit contains two Ca^{2+}-binding motifs: a C-terminal canonical EF-hand and an N-terminal pseudo EF-hand that is unique to S100 proteins (Bresnick *et al.*, 2015). Although S100 family members exhibit a high degree of sequence and structural similarity, they are not functionally interchangeable, and distinct S100 proteins participate in a wide range of biological processes, including proliferation, migration and/or invasion, inflammation, and differentiation (Marenholz *et al.*, 2004; Donato *et al.*, 2013). Functional diversity within the S100 family is accomplished through differences in the metal-binding properties of individual family members; their ability to form homodimers,

and in some cases, heterodimers; their interactions with distinct protein partners; and their distinct patterns of tissue/cell expression (Heizmann and Cox, 1998; Santamaria-Kisiel *et al.*, 2006; Donato *et al.*, 2013).

S100A4 is highly expressed in fibroblasts (Takenaga *et al.*, 1994) and immune cells, including monocytes and macrophages (Li *et al.*, 2010; Hashimoto *et al.*, 2013), T-cells (Weatherly *et al.*, 2015), and other bone marrow–derived cells (Erlandsson *et al.*, 2013; Scheiter *et al.*, 2013; Bruhn *et al.*, 2014). Furthermore, S100A4 expression in breast, lung, prostate, colorectal, and brain tumor cells has been linked to invasive behavior (Bresnick *et al.*, 2015). A major mechanism of S100A4 action in motile cells involves its regulation of actomyosin-mediated motility. Biochemical studies have shown that S100A4 binds with high affinity to the nonmuscle myosin-IIA heavy chain and mediates myosin-IIA filament depolymerization (Li *et al.*, 2003; Kiss *et al.*, 2012, 2016). Consistent with the biochemical activity of S100A4 in vitro, the loss of S100A4 results in myosin-IIA filament overassembly and a decrease in the migratory capacity of multiple cell types (Dulyaninova and Bresnick, 2013). Importantly, the binding of S100A4 to myosin-IIA is Ca^{2+} dependent. Thus, S100A4 functions as a calcium sensor whose regulation of the actomyosin cytoskeleton is linked to dynamic changes in intracellular calcium levels.

Our previous studies showed that bone marrow–derived macrophages (BMMs) isolated from mice with a genetic deletion of S100A4 exhibit defects in directional motility and chemotaxis in vitro and reduced thioglycollate-induced recruitment to the peritoneal cavity in vivo (Li *et al.*, 2010). The recruitment of inflammatory monocytes to sites of infection requires exit from the bone marrow and

Abbreviations used: 2D, two-dimensional; 3D, three-dimensional; ANOVA, analysis of variance; BFA, brefeldin A; BMM, bone marrow–derived macrophage; BSA, bovine serum albumin; CSF-1, colony-stimulating factor 1; DAPI, 4,6-diamidino-2-phenylindole; DMSO, dimethyl sulfoxide; MMP, matrix metalloprotease; PBS, phosphate-buffered saline.; PVDF, polyvinylidene difluoride; TBP, TATA-box-binding protein.

spleen, entry into the bloodstream, and migration across the endothelium at sites of infection (Shi and Pamer, 2011). Upon migration into infected tissue, monocytes differentiate into dendritic cells and classically activated M1 macrophages, and migrate though the dense extracellular matrix to confront pathogens. The ability of monocytes/macrophages to undergo transendothelial migration and invade target tissues depends on podosomes (Medina *et al.*, 2015). These actin-rich structures perform both adhesive and invasive functions, allowing macrophages to penetrate through endothelial layers and the extracellular matrix (Gimona *et al.*, 2008; Linder and Wiesner, 2015).

Podosomes contain an actin-rich core that is surrounded by a ring structure consisting of proteins associated with cellular adhesions (Linder *et al.*, 2011). Individual podosomes are linked by actomyosin filaments, and sensing of mechanical stress by the myosin-mediated contractile apparatus regulates podosome dynamics (Linder and Wiesner, 2016). Podosomes drive cell invasion by coupling actin-mediated protrusion to microtubule-mediated secretion of matrix metalloproteases (MMPs) (Wiesner *et al.*, 2010). Individual podosomes organize into larger structures called rosettes, whose appearance correlates with the ability to degrade extracellular matrix (Van Goethem *et al.*, 2011; Guiet *et al.*, 2012).

The formation of podosome rosettes is enhanced by calcium influx via specific ion channels (Clark *et al.*, 2006; Siddiqui *et al.*, 2012) and is disrupted by pharmacological inhibition of myosin-II (Collin *et al.*, 2006, 2008). Given that S100A4 is a Ca^{2+}-dependent regulator of myosin-IIA, we examined its role in the formation of matrix-degrading structures in BMMs. Our studies identify S100A4 as an important and novel regulatory component in the organization and degradative function of podosome rosettes in macrophages. Importantly, S100A4 acts through both myosin-IIA–dependent and myosin-IIA–independent mechanisms to regulate rosette size, degradative capacity, and dynamics, such that S100A4 loss leads to a profound defect in macrophage invasion.

RESULTS

S100A4 is required for macrophage invasion and regulates MMP9 secretion

Our previous studies showed that primary BMMs from S100A4$^{-/-}$ mice exhibit defects in colony-stimulating factor 1 (CSF-1)–stimulated chemotactic migration, due in part to myosin-IIA overassembly (Li *et al.*, 2010). In addition, these studies revealed that S100A4 deletion reduces macrophage recruitment in a thioglycollate-induced model of peritonitis. Consistent with our published in vivo recruitment studies, S100A4$^{-/-}$ BMMs exhibited a 44% reduction in Matrigel invasion (Figure 1).

While defects in the directional motility of S100A4$^{-/-}$ BMMs (Li *et al.*, 2010) could account for the observed reductions in invasion, we considered whether additional mechanisms might contribute to this phenotype. In particular, a number of studies have reported that S100A4 knockdown in tumor cells reduces MMP9 mRNA levels (Saleem *et al.*, 2006; Zhang *et al.*, 2011), and genetic deletion of MMP9 inhibits BMM invasion and matrix degradation (Fleetwood *et al.*, 2014). To evaluate whether alterations in MMP9 or other proteases contribute to the reduction in the invasive capacity of S100A4$^{-/-}$ BMMs, we used an angiogenesis antibody array. Conditioned medium derived from S100A4$^{-/-}$ BMMs contained increased levels of MMP8 and MMP9 compared with medium from wild-type BMMs (Figure 2A). These changes did not reflect a general effect on the secretory pathway, as few differences in other secreted proteins were observed (unpublished data). An examination of MMP9 by gelatin zymography also revealed a significantly increased accumu-
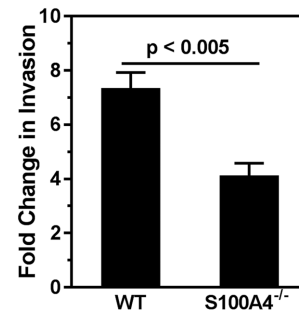
FIGURE 1: S100A4$^{-/-}$ BMMs exhibit reduced Matrigel invasion toward BMM growth medium. BMMs were starved for 5 h in serum and CSF-1–free complete BMM medium before being seeded into the upper chambers of 8-μm Transwells coated with growth factor–reduced Matrigel. Stimulated invasion is expressed as the fold change relative to unstimulated cells. The data represent the mean ± SEM from four independent experiments performed in duplicate. Statistical analysis was performed using an unpaired Student's *t* test.

lation of MMP9 in the conditioned media of S100A4$^{-/-}$ BMMs (Figure 2B). Consistent with these observations, an MMP9 activity assay that monitors MMP9 activity through cleavage of a chromogenic peptide substrate demonstrated a 55% increase in total MMP9 in the medium from S100A4$^{-/-}$ BMMs compared with wild-type BMMs (Figure 2C). In contrast to these assays reporting on MMP9 protein levels, quantitative real-time PCR (RT-qPCR) analysis did not reveal any significant differences in MMP9 mRNA between S100A4$^{-/-}$ and wild-type BMMs (Figure 2D).

MMP9 is known to be synthesized in a precursor form that is progressively converted to a fully glycosylated mature form (Olson *et al.*, 2000), and there can be significant heterogeneity with regard to the molecular weight of MMP9 species detected in a whole-cell lysate. Consistent with previous reports in mouse macrophages (Hanania *et al.*, 2012; Tauber *et al.*, 2012), immunoblot analysis of whole-cell lysates from S100A4$^{-/-}$ and wild-type BMMs revealed two MMP9 immunoreactive bands (Figure 2E). Densitometric analysis of these immunoblots indicated a reduction in total MMP9 in S100A4$^{-/-}$ BMMs (Figure 2F). Following brefeldin A (BFA) treatment, which disrupts anterograde secretory traffic through the Golgi apparatus, we observed a single immunoreactive MMP9 band that likely represents a partially glycosylated form of MMP9 (Figure 2G). Notably, BFA restored MMP9 levels in S100A4$^{-/-}$ BMMs to those observed for wild-type BMMs (Figure 2H). Taken together, these data suggest that the reduction in MMP9 levels in whole-cell lysates of S100A4$^{-/-}$ BMMs and the increased MMP9 in the medium of these cells are due to enhanced MMP9 secretion.

In macrophages, trafficking of MMP9-containing vesicles occurs along subsets of stabilized microtubules (Hanania *et al.*, 2012). Stable microtubules are known to accumulate posttranslational modifications, including acetylation (Janke and Bulinski, 2011), and K40 acetylation on α-tubulin can be used as a marker for stabilized microtubules. We observed a 43% increase in α-tubulin K40 acetylation in S100A4$^{-/-}$ BMMs compared with wild-type BMMs (Figure 3, A and B). Consistent with this observation, immunofluorescence studies revealed a more extensive microtubule network in S100A4$^{-/-}$ BMMs (Figure 3C) that was resistant to nocodazole-mediated depolymerization (Supplemental Figure 1). These data indicate that the microtubule network is more stable and less dynamic in S100A4$^{-/-}$ BMMs and suggest a correlation between stabilization of the microtubule network and MMP9 secretion in these cells.
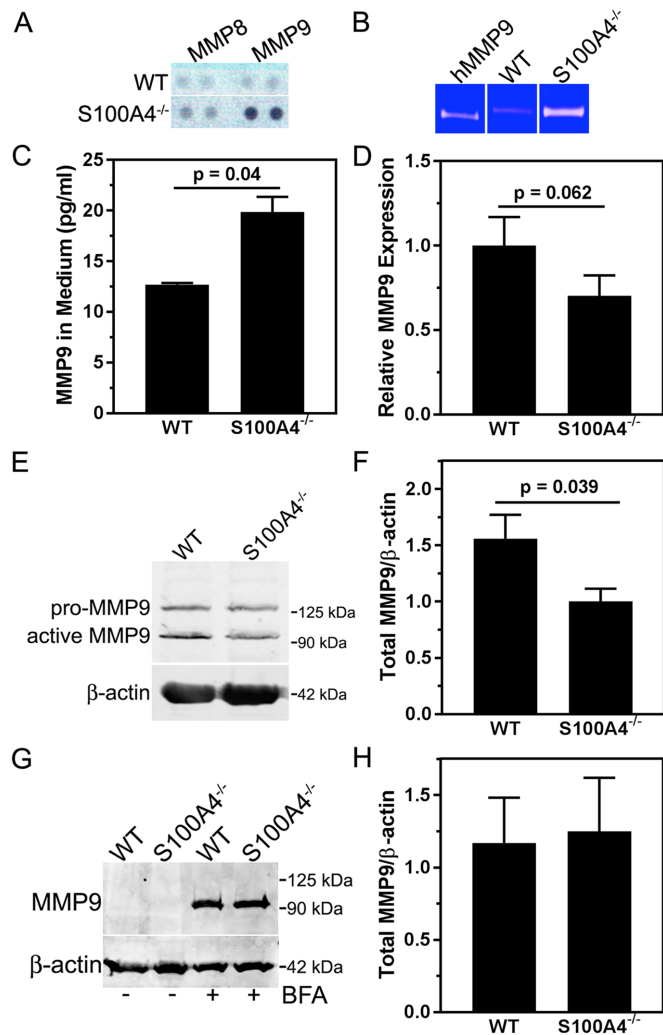
FIGURE 2: S100A4−/− BMMs exhibit increased MMP9 secretion. (A) Angiogenesis antibody array of conditioned medium from S100A4−/− and wild-type BMMs. On the array, the MMP8 antibody recognizes only the pro form of the protein, whereas the MMP9 antibody recognizes both the pro and active forms of the enzyme. (B) Gelatin zymography of MMP9 in conditioned media from S100A4−/− and wild-type BMMs. hMMP9: pro form of human MMP9 was used as a standard. (C) Biotrak MMP9 activity assay of total MMP9 in conditioned medium from S100A4−/− and wild-type BMMs. Data represent the mean ± SEM from three independent experiments. (D) RT-qPCR analysis of MMP9 expression in S100A4−/− and wild-type BMMs. Data represent the mean ± SEM from three independent assays performed in triplicate. (E) Representative immunoblot of MMP9 expression in whole-cell lysates from S100A4−/− and wild-type BMMs. (F) Quantification of total MMP9 levels in whole-cell lysates from S100A4−/− and wild-type BMMs. Data represent the mean ± SEM from seven independent blots. (G) Representative immunoblot of MMP9 expression in whole-cell lysates from BFA-treated S100A4−/− and wild-type BMMs. (H) Quantification of MMP9 levels in whole-cell lysates from BFA-treated S100A4−/− and wild-type BMMs. Data represent the mean ± SEM from three independent blots. Statistical analyses were performed using a two-tailed unpaired Student's t test.

S100A4 regulates podosome rosette-mediated gelatin degradation

The finding that S100A4−/− BMMs secreted more MMP9 was surprising, given that these cells exhibited defects in Matrigel invasion. To
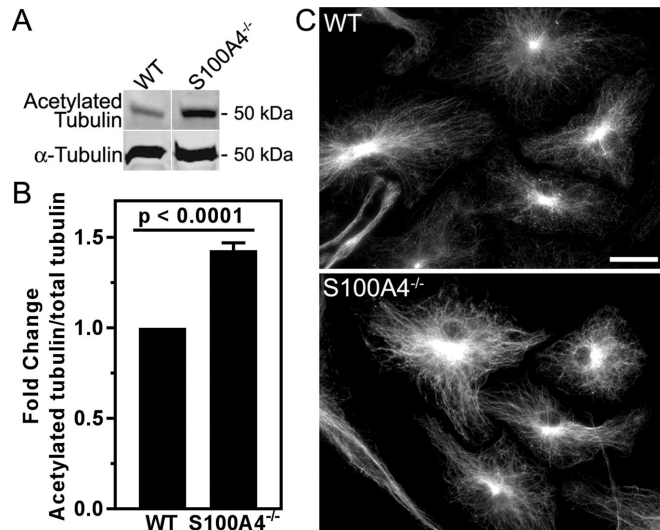
FIGURE 3: α-Tubulin K40 acetylation is elevated in S100A4−/− BMMs. (A) Representative immunoblot of α-tubulin K40 acetylation in whole-cell lysates from S100A4−/− and wild-type BMMs. (B) Quantification of α-tubulin K40 acetylation in whole-cell lysates from S100A4−/− and wild-type BMMs. Acetylation is expressed as the ratio of acetylated α-tubulin to total α-tubulin normalized to wild-type BMMs. Data represent the mean ± SEM from five independent blots. Statistical analysis was performed using an unpaired Student's t test. (C) α-Tubulin immunofluorescence of S100A4−/− and wild-type BMMs. Fluorescence micrographs were imaged under identical conditions. Scale bar: 20 μm.

further explore the mechanisms contributing to impaired invasion by S100A4−/− BMMs, we directly examined the capacity of these cells to degrade matrix. When cells were plated on a fluorescent gelatin substrate, the area of degraded matrix was reduced by 61% in S100A4−/− BMMs compared with wild-type BMMs (Figure 4, A and B). This suggests that MMP9 secretion by S100A4−/− BMMs is not effectively coupled to matrix degradation.

In murine bone marrow–derived macrophages, the formation of podosome rosettes is required for matrix degradation and three-dimensional migration (Cougoule et al., 2010). To determine whether the difference in the matrix degrading activity of S100A4−/− BMMs was due to alterations in podosome rosette formation, we examined the number and size of podosome rosettes. In cells plated overnight on gelatin, there was a 60% reduction in the number of S100A4−/− BMMs with podosome rosettes as compared with wild-type BMMs (Figure 5, A and B). In addition, an evaluation of rosette area revealed that S100A4−/− BMMs formed podosome rosettes that were 2.5-fold smaller than podosome rosettes in wild-type BMMs (Figure 5C).

When CSF-1 and serum starved wild-type BMMs were plated on gelatin, we observed that 69% of wild-type BMMs had podosome rosettes, whereas only 28% of S100A4−/− BMMs exhibited podosome rosettes (Figure 6, A and B, time 0 min). Stimulation with an equal volume of complete BMM medium (60 ng/ml CSF-1 and 7.5% serum final concentration) induced the rapid disassembly of podosome rosettes in wild-type BMMs, with only 5% of cells exhibiting rosettes 10 min after stimulation. In contrast, S100A4−/− BMMs exhibited a delay in rosette disassembly, with 19 and 7.7% of S100A4−/− BMMs exhibiting podosome rosettes 10 and 20 min after simulation, respectively (Figure 6, A and B). These data demonstrate that not only do S100A4−/− BMMs have fewer and smaller podosome rosettes, but the kinetics of rosette disassembly is slowed.
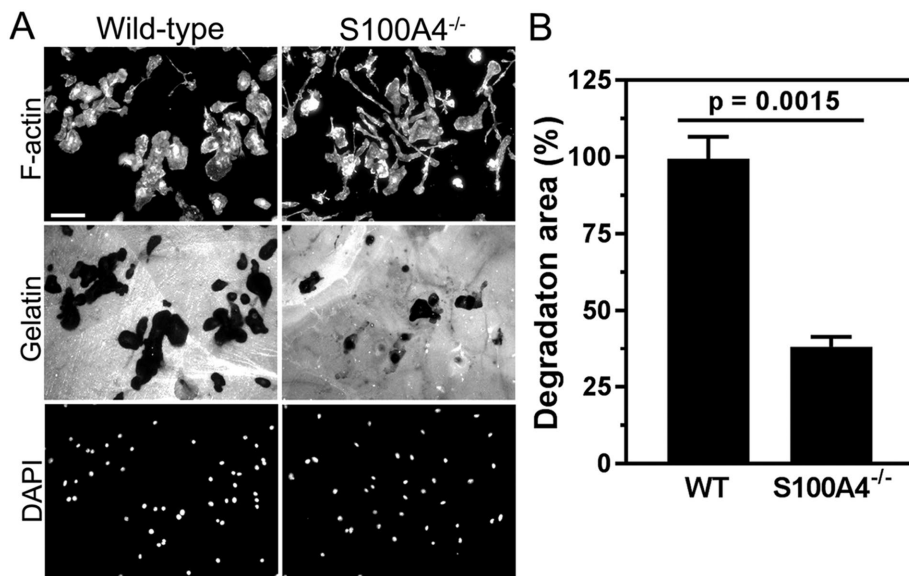
FIGURE 4: S100A4⁻/⁻ BMMs are deficient in matrix degradation. (A) Representative images of matrix degradation assay for S100A4⁻/⁻ and wild-type BMMs. Following culture on Oregon Green 488 gelatin for 17 h, cells were fixed and stained for F-actin and nuclei to quantify matrix degradation. Scale bar: 50 μm. (B) Quantification of Oregon Green 488 gelatin degradation by S100A4⁻/⁻ and wild-type BMMs. Data represent the mean ± SEM from three independent experiments. Statistical analysis was performed using an unpaired Student's *t* test.

Blebbistatin treatment rescues defects in podosome organization and matrix degradation

Our biochemical studies previously showed that myosin-IIA is over-assembled in S100A4⁻/⁻ BMMs (Li *et al.*, 2010). Consistent with these data, myosin-IIA exhibited a linear punctate pattern in the cortex of S100A4⁻/⁻ BMMs that was not observed in wild-type BMMs (Figure 7A). Although myosin-IIA is not a component of the podosome core, it localizes to the radial F-actin network that surrounds individual podosomes (Bhuwania *et al.*, 2012), and actomyosin filaments regulate the organization of podosome clusters in dendritic cells (Meddens *et al.*, 2016). An examination of podosome rosettes revealed that myosin-IIA is highly enriched in these structures (Figure 7B). Despite the extensive myosin-IIA filaments detected in the cortex of S100A4⁻/⁻ BMMs, we did not observe any gross alterations in the localization or organization of myosin-IIA within the small podosome rosettes in these cells.

We have previously shown that low doses of blebbistatin, a small molecule inhibitor that stabilizes the myosin-II motor in a weak actin-binding state (Kovacs *et al.*, 2004; Limouze *et al.*, 2004), can counteract the actomyosin overassembly induced by S100A4 loss (Li *et al.*, 2010). We therefore used blebbistatin as a tool to probe for myosin-IIA–dependent and myosin-IIA–independent mechanisms with respect to MMP9 secretion and matrix degradation in S100A4⁻/⁻ BMMs. Treatment of S100A4⁻/⁻ BMMs with the active isomer of blebbistatin increased the matrix degradation area to 90% of that seen in untreated wild-type BMMs (Figure 8A). In addition, blebbistatin increased the area of podosome rosettes in S100A4⁻/⁻ BMMs to levels that were comparable to the average rosette area in wild-type BMMs (Figure 8B).

Myosin-IIA–independent regulation of microtubule acetylation and invasion by S100A4

Surprisingly, despite the restoration of matrix degradation and podosome rosette size in blebbistatin-treated S100A4⁻/⁻ BMMs, blebbistatin did not rescue the defect in Matrigel invasion observed for

these cells (Figure 8C). These data suggest that, while S100A4 regulates macrophage invasion in part through a myosin-IIA–dependent effect on podosome rosette formation and matrix degradation, additional myosin-IIA–independent functions of S100A4 are required for Matrigel invasion.

Treatment of S100A4⁻/⁻ BMMs with 5 μM blebbistatin did not affect the levels of MMP9 secretion or α-tubulin K40 acetylation compared with cells that were treated with an inactive isomer of blebbistatin (Supplemental Figures 2 and 3). We therefore tested whether the myosin-IIA–independent role for S100A4 in Matrigel invasion could involve α-tubulin K40 acetylation. To determine whether alterations in tubulin acetylation affect the invasive capacity of wild-type BMMs, we treated wild-type BMMs with tubacin, an HDAC6-selective inhibitor. Doses of 2.5–5 μM tubacin increased α-tubulin K40 acetylation in wild-type BMMs to levels observed in S100A4⁻/⁻ BMMs (Figure 9, A and B). This increase in tubulin acetylation resulted in the stabilization of podosome rosettes to serum/CSF-1–mediated disassembly (Figure 9C), similar to what was seen in S100A4⁻/⁻ BMMs (Figure 6B), and also correlated with a 30–50% reduction in the invasion of wild-type BMMs (Figure 9D) that was comparable to the decrease in invasion observed for S100A4⁻/⁻ BMMs (Figure 1). Higher levels of microtubule acetylation (unpublished data) and greater reductions in invasion (Figure 9D) were seen with 25 μM tubacin. These data demonstrate that posttranslational modification of microtubules is a critical regulator of BMM invasion, as increases in microtubule acetylation by S100A4 loss or tubacin treatment are sufficient to inhibit invasion.

DISCUSSION

In this study, we demonstrate that S100A4, a Ca²⁺-regulated mediator of myosin-IIA assembly, modulates the matrix-degrading capacity of macrophages via both myosin-IIA–dependent and myosin-IIA–independent mechanisms. Studies in a number of cell types have suggested that calcium influx mediates the assembly and activity of invadopodia and podosomes (Miyauchi *et al.*, 1990; Siddiqui *et al.*, 2012; Sun *et al.*, 2014). Although the direct visualization of localized calcium signals in association with these matrix-degrading structures has been elusive (Visser *et al.*, 2013), more recent studies have identified calcium oscillations as critical for invadopodium precursor assembly (Sun *et al.*, 2014). Moreover, in macrophages, calcium influx supports short-lived calcium transients at the leading edge of polarized cells (Evans and Falke, 2007) where podosomes and podosome rosettes reside (Evans *et al.*, 2003; Siddiqui *et al.*, 2012). Consistent with their regulation by calcium, podosomes and invadopodia have been reported to be modulated by a number of calcium channels, including the store-operated calcium channel Orai1, the calcium release–activated calcium channel, and small-conductance calcium-activated potassium channels (Siddiqui *et al.*, 2012; Sun *et al.*, 2014), as well as Ca²⁺-regulated proteins such as calpain, Pyk2, calmodulin, Iba1 (Calle *et al.*, 2006; Gil-Henn *et al.*, 2007; Siddiqui *et al.*, 2012), and now S100A4.

Podosomes are recognized as mechanosensors whose activity and dynamics are modulated by actomyosin contractility
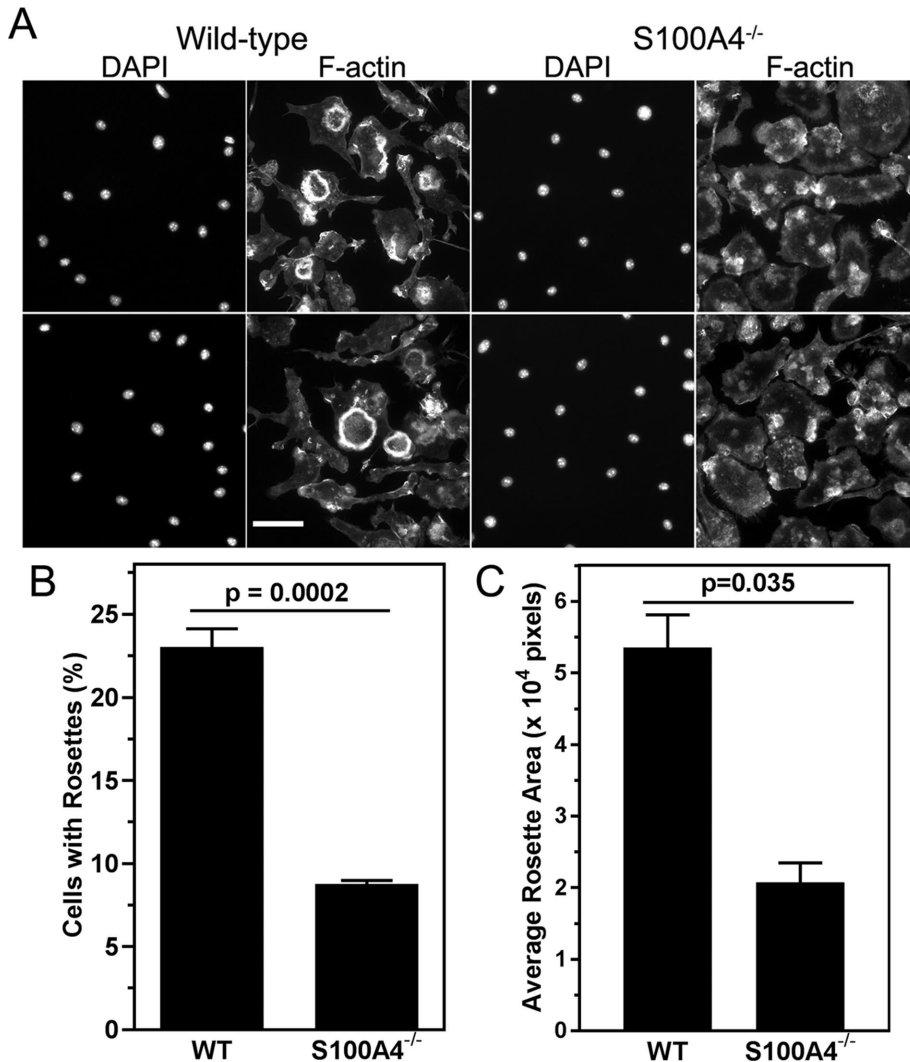
FIGURE 5: S100A4$^{-/-}$ BMMs form fewer and smaller podosome rosettes. (A) Representative images of podosome rosettes for S100A4$^{-/-}$ and wild-type BMMs. Following culture on Oregon Green 488 gelatin for 17 h, cells were fixed and stained for F-actin and nuclei. Scale bar: 50 μm. (B) Quantification of percent S100A4$^{-/-}$ and wild-type BMMs with podosome rosettes. Data represent the mean ± SEM from three independent experiments. (C) Quantification of podosome rosette area in S100A4$^{-/-}$ and wild-type BMMs. Data represent the mean ± SEM from three independent experiments. Statistical analyses were performed using a two-tailed unpaired Student's t test.

Mitsuhashi *et al.*, 2011), disrupts podosome rosette structure and function. These studies show that the regulation of myosin-IIA filament assembly through heavy chain–directed mechanisms is critical for tuning actomyosin contractility, which could impact individual podosomes via the modulation of oscillatory behavior (van den Dries *et al.*, 2013; Labernadie *et al.*, 2014) and the organization of podosomes into higher-order structures such as clusters and rosettes (Meddens *et al.*, 2016).

Our studies with blebbistatin also reveal myosin-IIA–independent effects of S100A4 loss that include enhanced α-tubulin K40 acetylation and MMP9 secretion. Because microtubule acetylation stimulates the trafficking of kinesin-associated vesicles in vivo (Bhuwania *et al.*, 2014) and MMP9-containing vesicles traffic along stabilized microtubules (Hanania *et al.*, 2012), we suspect that the increase in MMP9 secretion is likely a secondary consequence of the increase in microtubule acetylation and stability observed in S100A4$^{-/-}$ BMMs.

How might loss of S100A4 modulate microtubule acetylation? Microtubule acetylation is stimulated by the acetyltransferase α-TAT1 (MEC-17) and inhibited by the deacetylases HDAC6 and Sirtuin-2 (North *et al.*, 2003; Sadoul and Khochbin, 2016). Paxillin, a focal adhesion– and podosome-associated scaffold protein, has been shown to regulate microtubule acetylation by directly inhibiting HDAC6 (Deakin and Turner, 2014). We have previously shown that S100A4 deletion has profound effects on paxillin (Li *et al.*, 2010): pY118-paxillin is increased in CSF-1–stimulated S100A4$^{-/-}$ BMMs, and there is a dramatic decrease in pY118-paxillin associated with detergent-resistant cytoskeletons. This suggests that S100A4 may play a role in the targeting of paxillin to cytoskeletal structures, which could impact HDAC6 localization or activity.

In addition, S100A4 could regulate microtubule dynamics via interactions with liprin β1 (Kriajevska *et al.*, 2002), a scaffolding protein associated with cortical assemblies that cluster near focal adhesions to mediate microtubule stability (van der Vaart *et al.*, 2013; Chiaretti and de Curtis, 2016; Dong *et al.*, 2016). Recent studies have identified liprin β1 as a Sirtuin-2–interacting protein (Budayeva and Cristea, 2016). While it is not known how liprin β1 regulates Sirtuin-2, loss of S100A4 could affect liprin β1/Sirtuin-2 interactions and Sirtuin-2 activity or subcellular targeting. Thus, S100A4 could modulate microtubule acetylation through a number of mechanisms whose investigation is beyond the scope of the current study.

While the precise link between S100A4 and microtubule acetylation remains unknown, changes in microtubule stability could dramatically affect podosome dynamics and their organization into higher-order structures like rosettes. At the level of individual podosomes, microtubule acetylation decreases microtubule–podosome contacts and delivery of MMP-containing vesicles and

(Linder and Wiesner, 2016). Mechanosensing is mediated by two populations of actomyosin filaments: lateral filaments within individual podosomes that link the top of the podosome core to the adhesion protein ring structure and filaments that connect individual podosomes into higher-order superstructures (Linder and Wiesner, 2015). An appropriate balance of actomyosin contractility is critical for the maintenance of podosomes, as podosome dissolution is caused by disruption of myosin-II binding to F-actin by blebbistatin or inhibition of myosin regulatory light-chain phosphorylation (Kopp *et al.*, 2006; Collin *et al.*, 2008; van Helden *et al.*, 2008). Similarly, podosome formation is inhibited by expression of kinase-dead TRPM7, a cation channel fused to an α-kinase that phosphorylates the myosin-IIA heavy chain to mediate myosin-IIA filament disassembly (Clark *et al.*, 2006, 2008). We now demonstrate that loss of S100A4, which binds to the C-terminal end of the myosin-IIA heavy chain in a Ca^{2+}-dependent manner and disassembles myosin-IIA filaments (Li *et al.*, 2003, 2010;

FIGURE 6: Podosome rosettes are more stable in S100A4^{−/−} BMMs. (A) Representative images of podosome rosette disassembly in S100A4^{−/−} and wild-type BMMs. BMMs were serum and CSF-1 starved, plated on gelatin, and then stimulated with medium (final concentrations: 60 ng/ml CSF-1 and 7.5% serum). Starved BMMs (0 min) have rosettes (arrows), which disassemble into individual podosomes (F-actin punctae). Inset: individual podosomes within a rosette. Scale bar: 50 μm. (B) Quantification of percent of S100A4^{−/−} and wild-type BMMs with podosome rosettes. Data represent the mean ± SEM from three independent experiments. Inset: the number of cells with rosettes plotted as a percent of the number at $t = 0$.

also decreases podosome number in human macrophages (Bhuwania et al., 2014). While this might suggest that disruption of microtubule–podosome contacts is responsible for impaired invasion in S100A4^{−/−} BMMs, blebbistatin rescues matrix degradation by individual podosomes but does not rescue invasion.

The finding that S100A4 loss stabilizes podosome rosettes, as does tubacin treatment of wild-type macrophages, suggests an alternative hypothesis, in which the stabilization of podosome rosettes inhibits three-dimensional (3D) invasion. Consistent with this idea, microtubule destabilization in human primary macrophages promotes podosome disassembly (Linder et al., 2000). Furthermore, in osteoclasts, where podosomes assemble into peripheral belts that form sealing rings required for degradation of bone matrix, microtubule acetylation increases the formation of podosome belts (Biosse Duplan et al., 2014) and enhances belt stability (Destaing et al., 2005). Similarly, loss of microtubule acetylation in Pyk2^{−/−} osteoclasts is associated with decreased podosome-belt formation (Gil-Henn et al., 2007). In these studies, podosome-belt stabilization caused by microtubule acetylation correlates with an increase in two-dimensional (2D) matrix degradation. However under 2D culture conditions on calcite, the podosome belts observed in osteoclasts are relatively stable structures (Batsir et al., 2017), perhaps due to the high density of the extracellular matrix they encounter (Collin et al., 2006). In contrast, in Src-transfected fibroblasts plated on gelatin or transforming growth factor β1–stimulated THP-1 cells plated on fibronectin, podosome rosettes and superstructures are highly dynamic, with striking changes in both shape and localization within the seconds to minutes timescale (Cox et al., 2011; Kedziora et al., 2016). While stabilization of podosome rosettes by microtubule acetylation in osteoclasts might increase rosette degradative capacity, human macrophages moving through a 3D collagen gel rapidly disassemble and reassemble podosomes (lifetime of ~5 min) (Van Goethem et al., 2011), and enhanced stabilization of rosettes could interfere with this remodeling. This is analogous to observations from NIH 3T3 cells, in which microtubule acetylation increases the stability of focal adhesions and decreases invasion (Tran et al., 2007). In future experiments, live-cell imaging of podosome rosettes will test whether a disruption of rosette dynamics is responsible for the reduced invasion by S100A4^{−/−} BMMs.

In summary, we find that S100A4 plays complex roles in the regulation of macrophage function. The defect in invasion by S100A4^{−/−} BMMs involves S100A4 regulation of both the actomyosin and microtubule cytoskeletons. The myosin-IIA–dependent and myosin-IIA–independent functions of S100A4 appear to converge on the regulation of podosome rosettes, and the formation and dynamics of these structures emerge as critical regulators of macrophage motility and invasion.

MATERIALS AND METHODS
Antibodies and reagents
The nonmuscle myosin-IIA rabbit antibody was from Biomedical Technologies (cat. no. BT-567). Vinculin (cat. no. V9131), β-actin (cat. no. A1978), α-tubulin (cat. no. T6074), and acetylated K40 α-tubulin (cat. no. T7451) antibodies were from Sigma. The MMP9 polyclonal antibody against the catalytic domain of rat MMP9 was from Millipore (cat. no. AB19016). The MMP9 polyclonal antibody against mouse full-length MMP9 (Ala-20–Pro-730) was from R&D Systems (cat. no. AF909-SP). Recombinant human proMMP9 (93 kDa) was from R&D Systems (cat. no. 911-MP-010). Rhodamine phalloidin was from Invitrogen. The active and inactive blebbistatin
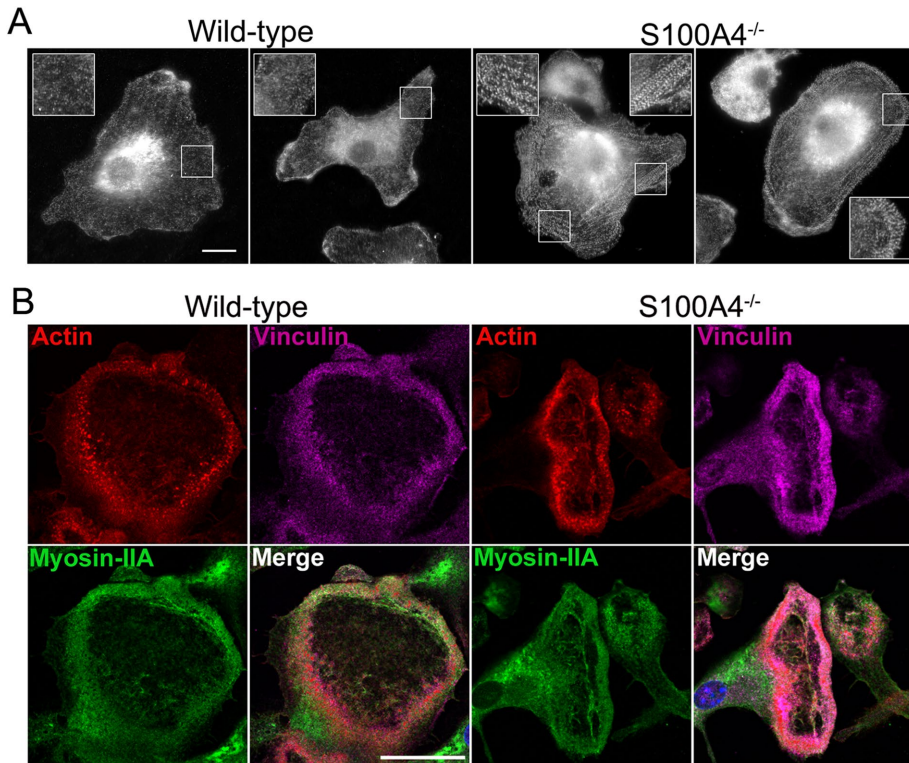
FIGURE 7: Myosin-IIA organization is altered in S100A4$^{-/-}$ BMMs. (A) Representative epifluorescence images of S100A4$^{-/-}$ and wild-type BMMs stained with antibodies to myosin-IIA. Cortical myosin-IIA is increased in S100A4$^{-/-}$ BMMs (boxes). Scale bar: 10 μm. (B) Representative confocal slices of podosome rosettes in S100A4$^{-/-}$ and wild-type BMMs. Cells were stained with phalloidin (red) and antibodies to vinculin (purple) and myosin-IIA (green). Scale bar: 25 μm.

isomers were purchased from Calbiochem; and BFA, tubacin, and nocodazole were purchased from Sigma.

Isolation of bone marrow–derived macrophages

S100A4$^{-/-}$ mice were maintained and bred in a pathogen-free barrier facility. All experiments were performed according to protocols approved by the Animal Welfare Committee at the Albert Einstein College of Medicine. BMMs were isolated from 12- to 14-wk-old mice as described previously (Li *et al.*, 2010). Mature macrophages were cultured in complete BMM medium (α-MEM containing 0.02 mg/ml asparagine, 2 mM L-glutamine, 100 U/ml penicillin G, 100 μg/ml streptomycin sulfate, 15% fetal bovine serum, and 10,000 U/ml human recombinant CSF-1 [kindly provided by E. Richard Stanley, Albert Einstein College of Medicine]). Day 8–11 BMMs were used for all experiments.

Transwell invasion assays

BMMs were starved for 5 h in serum and CSF-1–free complete BMM medium. In all, 100,000 BMMs were seeded into the upper chambers of 8-μm Transwells coated with growth factor–reduced Matrigel (Bio-Coat #354483, Corning) in 400 μl of starvation medium. The Transwells were placed into a 24-well plate containing 500 μl of complete BMM medium, and the cells were allowed to migrate for 24 h at 37°C. For control samples, starvation medium was placed into the lower wells. For invasion assays in the presence of blebbistatin, 5 μM of the active (–) or inactive (+) isomer was added to both the upper and lower wells. For invasion assays in the presence of tubacin, 2.5, 5, or 25 μM tubacin was added to both the upper and lower wells. After

invasion, cells on the upper surface of the membrane were removed with a cotton swab. Cells on the lower surface of the membrane were fixed with 3.7% formaldehyde in phosphate-buffered saline (PBS) for 10 min and stained with 4,6-diamidino-2-phenylindole (DAPI). After three PBS washes, the membranes were mounted onto slides using DAPI Fluoromount-G (Southern Biotech). Images from 10 random fields of cells on the underside of the membrane were taken using an UPlanFl 10×, 0.3 NA objective. ImageJ (National Institutes of Health) was used for automated counting of nuclei by setting up a threshold. Each nucleus present on the lower surface of each Transwell was scored as one invasion event. Invasion toward complete BMM medium was expressed as the fold change relative to invasion in the absence of serum and CSF-1 in the lower well.

Antibody arrays

Mouse Angiogenesis Proteome Profiler Arrays were purchased from R&D Systems (ARY015). Conditioned medium was prepared from 1.5×10^6 BMMs seeded onto 60-mm tissue-culture plates. Cells were allowed to attach and washed three times with PBS, and 2 ml of serum-free complete BMM medium was added to the plate. After 24 h, conditioned medium was collected, filtered with a 0.22-μm Millex-GV filter unit, and concentrated approximately eightfold with an Amicon Ultra Centrifugal Filter (3000-Da molecular weight cutoff). The antibody arrays were used to analyze the conditioned media according to the manufacturer's protocol.

Gelatin zymography

Conditioned medium was prepared as described in the preceding section. Samples were diluted in nonreducing sample buffer and separated on a 9.5% Tris-Tricine gel (0.95 M Tris, 0.10% SDS, 0.95% glycerol) containing 0.1% gelatin with a running buffer that contained 0.1 M Tris, 0.1 M Tricine, and 0.1% SDS. Gels were then washed twice for 30 min each in 2.5% Triton X-100 and incubated overnight at 37°C in developing buffer (50 mM Tris, pH 7.5, 150 mM NaCl, 5 mM CaCl$_2$, 0.02% NaN$_3$, and 5 μM ZnCl$_2$.). Gels were Coomassie stained for 1 h and then destained until areas of degraded gelatin became visible.

MMP9 activity assay

MMP9 activity in conditioned media collected from BMMs (as described earlier) was determined using the MMP9 Biotrak Activity Assay (GE Healthcare Life Sciences) following the manufacturer's protocol. For measurement of total MMP9 activity (pro- and active MMP9), 1 mM *p*-aminophenylmercuric acetate was added to the samples. An MMP9 standard curve (0.00625–0.05 ng of recombinant human proMMP9) was used to determine the concentration of active MMP9 in the conditioned media.

RNA isolation and RT-qPCR

RNA was purified with TriPure (Roche) according to the manufacturer's protocol and reverse transcribed with Moloney murine
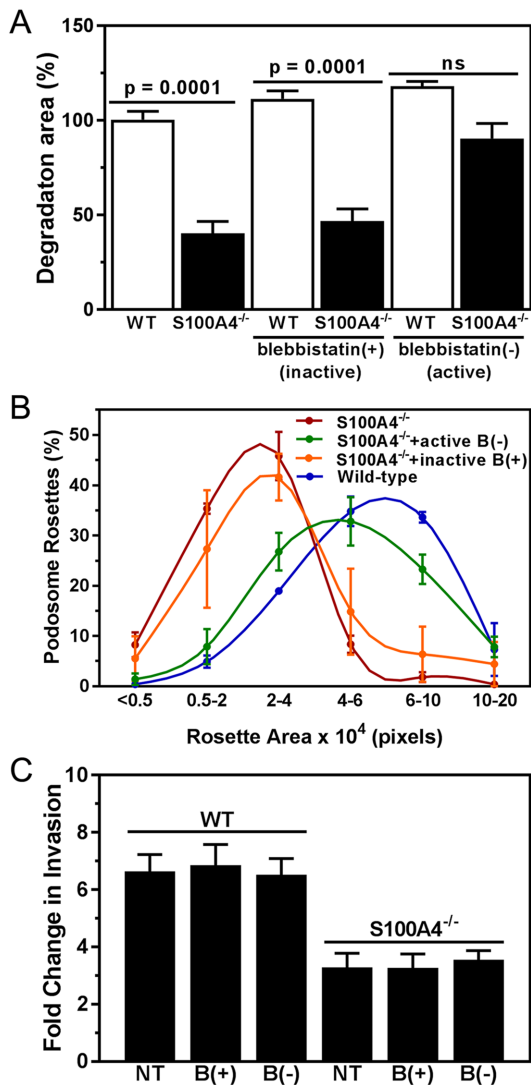
FIGURE 8: Blebbistatin treatment restores matrix degradation and podosome rosette area but not Matrigel invasion in S100A4$^{-/-}$ BMMs. (A) Quantification of Oregon Green 488 gelatin degradation by S100A4$^{-/-}$ and wild-type BMMs. Data represent the mean ± SEM from three independent experiments. Statistical analysis was performed using one-way analysis of variance (ANOVA). (B) Distribution of podosome rosette area in S100A4$^{-/-}$ and wild-type BMMs. Red line: untreated S100A4$^{-/-}$ BMMs; blue line: untreated wild-type BMMs; orange line: S100A4$^{-/-}$ BMMs treated with the inactive isomer of blebbistatin (+); green line: S100A4$^{-/-}$ BMMs treated with the active isomer of blebbistatin (−). Data represent the mean ± SEM from two to four independent experiments. (C) Matrigel invasion of S100A4$^{-/-}$ and wild-type BMMs toward growth medium. BMMs were starved for 5 h in serum and CSF-1–free complete BMM medium before being seeded into the upper chambers of 8-μm Transwells coated with growth factor–reduced Matrigel. Stimulated invasion is expressed as the fold change relative to unstimulated cells. NT, not treated; B(+), inactive isomer of blebbistatin; B(−), active isomer of blebbistatin. Data represent the mean ± SEM from three independent experiments performed in duplicate. Statistical analysis was performed using one-way ANOVA.

leukemia virus reverse transcriptase (Invitrogen) and a dT$_{18}$ primer. cDNA was purified using standard phenol chloroform extraction and ethanol precipitation to permit a higher concentration of cDNA in the RT-qPCR. cDNA, SYBR Green PCR master mix, and

forward and reverse primers were used in 45 cycles of amplification (95°C for 15 s, 60°C for 1 min) followed by a 10-min incubation at 95°C with a LightCycler 480 (Roche). The efficiency-corrected threshold cycle (ΔCT) method was used to calculate the relative levels of RNA (Schefe et al., 2006). The expression of MMP9 was normalized to TATA-box-binding protein (TBP). Specific primers were designed for MMP9 and TBP; MMP9 forward primer: 5'-CAGACCAAGGGTACAGCCTG-3', and MMP9 reverse primer: 5'-ATACAGCGGGTACATGAGCG-3'; TBP forward primer: 5'-TC-TACCGTGAATCTTGGCTGTAAA-3', and TBP reverse primer: 5'-TTCTCATGATGACTGCAGCAAA-3'. Each experiment was performed in triplicate. Melting-curve analysis was performed to ensure primer specificity.

Immunoblots

For acetylated α-tubulin/total α-tubulin immunoblots, cells were seeded as described for the gelatin zymography. After 24 h in serum-free complete BMM medium, cells were washed with PBS, and the plates were quickly frozen on dry ice. The cells were then lysed by scraping into 2X Laemmli sample buffer supplemented with 5 μg/ml each of chymostatin, leupeptin, pepstatin A, 1 mM phenyl-methylsulfonyl fluoride, and benzonase. Samples were separated by 12% Tris-Tricine SDS–PAGE and transferred to Immobilon-FL polyvinylidene difluoride (PVDF; Millipore), followed by immunoblotting with tubulin antibodies. The relative amounts of acetylated α-tubulin/total α-tubulin were estimated by densitometry using ImageQuant version 5.0. When indicated, the cells were treated with dimethyl sulfoxide (DMSO) or tubacin (2.5 or 5 μM) overnight.

For MMP9 immunoblots, 750,000 BMMs were plated on 60 mm tissue culture dishes in complete BMM medium. After 4 h, cells were washed three times with PBS and incubated in serum-free complete BMM medium with or without 500 ng/ml BFA overnight. Protein samples were prepared as described in the preceding section. Samples were separated by 10% SDS–PAGE, transferred to Immobilon-FL PVDF, and probed with MMP9 antibodies. Two different MMP9 antibodies were used for immunoblots. MMP9 from BFA-treated cells could only be detected with the MMP9 antibody from R&D Systems, which was made against mouse full-length MMP9. However, this antibody poorly recognizes the pro- and active forms of MMP9 in untreated cells. The MMP9 antibody from Millipore, made against the MMP9 catalytic domain, was used to detect pro- and active MMP9 in cell lysates from untreated cells.

Immunofluorescence and microscopy

Typically, cells were fixed in 3.7% formaldehyde in PBS for 15 min and permeabilized with 0.5% Triton X-100 in fixative for 3 min. For immunostaining of α-tubulin, cells were fixed and permeabilized in 100% methanol for 20 s at −20°C. For studies evaluating nocodazole-mediated microtubule depolymerization, cells were treated with 10 μM nocodazole for 5 min before fixation. Cells were blocked in PBS containing 1% bovine serum albumin (BSA) for 1 h and incubated with primary antibodies in PBS containing 1% BSA for 1 h using the following final dilutions: α-tubulin (1:200), myosin-IIA (1:100), and vinculin (1:200). Cells were then incubated with fluorochrome-conjugated secondary antibodies (1:500) and rhodamine phalloidin (1:300) in PBS containing 1% BSA for 30 min. Coverslips were mounted using DAPI Fluoromount-G.

Epifluorescence images were acquired with a Plan-Apo 60×, 1.4 NA objective (Olympus) and HiQ band-pass filters (Chroma Technology). All images were acquired using MetaMorph software and a CoolSNAP HQ interline 12-bit, cooled CCD camera
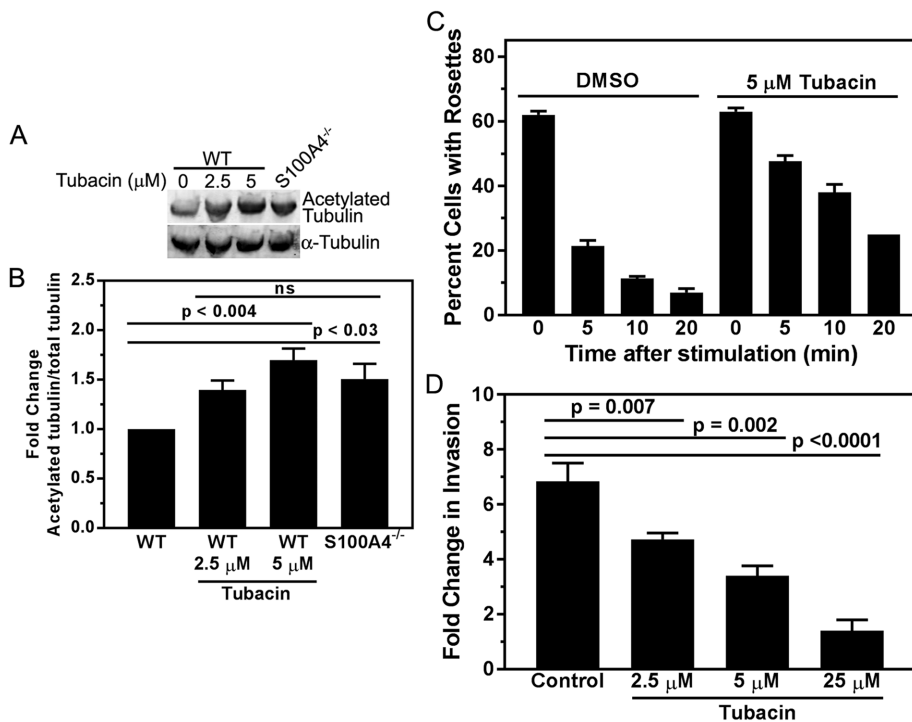
FIGURE 9: Tubacin treatment inhibits Matrigel invasion of wild-type BMMs. (A) Representative immunoblot of α-tubulin K40 acetylation in whole-cell lysates from wild-type BMMs treated with DMSO or tubacin and from untreated S100A4$^{-/-}$ BMMs. (B) Quantification of α-tubulin K40 acetylation in whole-cell lysates from untreated and tubacin-treated wild-type BMMs and untreated S100A4$^{-/-}$ BMMs. Acetylation is expressed as the ratio of acetylated α-tubulin to total α-tubulin normalized to wild-type BMMs. Data represent the mean ± SEM from four independent blots. Statistical analysis was performed using one-way ANOVA. (C) Rosette disassembly assay. Wild-type BMMs were starved, plated, treated with DMSO or 5 μM tubacin for 90 min, and stimulated as in Figure 6B. Data represent the mean ± SEM from three independent experiments. (D) Matrigel invasion of tubacin-treated wild-type BMMs toward growth medium. BMMs were starved for 5 h in serum and CSF-1–free complete BMM medium before being seeded into the upper chambers of 8-μm Transwells coated with growth factor–reduced Matrigel, in the presence of DMSO or 2.5–25 μM tubacin. Stimulated invasion is expressed as the fold change relative to unstimulated cells. Control: vehicle-treated BMMs. Data represent the mean ± SEM from three independent experiments performed in duplicate. Statistical analysis was performed using one-way ANOVA.

fluorescence. The percent degradation area was defined as the total degraded area per field divided by the total cell area per field based on rhodamine phalloidin staining. The number of cells in the field was determined by counting DAPI-stained nuclei. Three independent experiments were performed with a minimum of 700 cells per condition examined for each experiment. For studies with blebbistatin, cells were incubated overnight with 5 μM of the active (–) or inactive (+) isomers of blebbistatin. Three independent experiments were performed with a minimum of 230 cells per condition examined for each experiment.

Analysis of podosome rosette formation and size

BMMs were treated, plated, fixed, and stained as described for gelatin degradation assays. At least 20 fields per condition were imaged using an UPlanFl 20×, 0.3 NA objective and 1.5× magnification. Podosome rosettes were defined as ring-like structures composed of podosomes. The number of podosome rosettes per field was divided by the total cell number per field, which was determined by DAPI staining. Three independent experiments were performed with a minimum of 460 cells per condition examined for each experiment.

For the analysis of podosome rosette size, BMMs were cultured overnight on 200 μg/ml gelatin, fixed, and stained with rhodamine phalloidin and DAPI. For studies with blebbistatin, cells were incubated overnight with 5 μM of the active (–) or inactive (+) isomers of blebbistatin. At least 20 fields per condition were imaged using a Plan-Apo 60×, 1.4 NA objective. The area (in pixels) of podosome rosettes was measured using ImageJ software and the Trace tool. Three independent experiments were performed with a minimum of 86 rosettes per condition traced in each experiment.

Podosome disassembly assays

BMMs were serum and CSF-1 starved for 2 h and then plated on 200 μg/ml gelatin in starvation medium for 1 h to allow cells to form podosome rosettes. BMMs were then stimulated by the addition of an equal volume of complete BMM medium (60 ng/ml CSF-1 and 7.5% serum final concentration) to promote rosette disassembly. For studies with tubacin, cells were incubated with DMSO or 5 μM tubacin for 90 min before stimulation. Cells were fixed before stimulation (0 min) and at 5, 10, and 20 min after stimulation, and then stained with rhodamine phalloidin and DAPI. At least 15 fields per condition were imaged using a Plan-Apo 60×, 1.4 NA objective. The number of podosome rosettes per field were counted and divided by the total cell number per field. Three independent experiments were performed with a minimum of 70 cells per time point examined for each experiment.

(Roper Scientific) mounted on an Olympus IX70 microscope. Images were processed using Photoshop (Adobe Systems) or ImageJ. Confocal fluorescence images of fixed samples (0.29-μm sections) were acquired with a Leica TCS SP5 AOBS confocal scanning microscope equipped with a 63×, 1.4 NA objective.

Gelatin degradation assays

Acid-washed glass coverslips were treated with 0.01% poly-L-lysine for 10 min at room temperature followed by washing with PBS. Coverslips were then coated with 200 μg/ml Oregon Green 488–conjugated gelatin (Life Technologies) for 15 min at room temperature and washed extensively with PBS. BMMs were starved in serum-free complete BMM medium for 3 h, and then 1.5 × 10^5 BMMs were plated on the coverslips in the same medium. After 1 h, serum was added, and the cells were incubated for an additional 17 h. Cells were then fixed with 3.7% paraformaldehyde in PBS for 15 min and stained with rhodamine phalloidin and DAPI. At least 10–20 fields per condition were imaged using an UPlanFl 20×, 0.3 NA objective. The degradation area per field was measured by thresholding the images using ImageJ software to determine the total area in the field that lacked

REFERENCES

Batsir S, Geiger B, Kam Z (2017). Dynamics of the sealing zone in cultured osteoclasts. Cytoskeleton (Hoboken) 74, 72–81.

Bhuwania R, Castro-Castro A, Linder S (2014). Microtubule acetylation regulates dynamics of KIF1C-powered vesicles and contact of microtubule plus ends with podosomes. Eur J Cell Biol 93, 424–437.

Bhuwania R, Cornfine S, Fang Z, Kruger M, Luna EJ, Linder S (2012). Supervillin couples myosin-dependent contractility to podosomes and enables their turnover. J Cell Sci 125, 2300–2314.

Biosse Duplan M, Zalli D, Stephens S, Zenger S, Neff L, Oelkers JM, Lai FP, Horne W, Rottner K, Baron R (2014). Microtubule dynamic instability controls podosome patterning in osteoclasts through EB1, cortactin, and Src. Mol Cell Biol 34, 16–29.

Bresnick AR, Weber DJ, Zimmer DB (2015). S100 proteins in cancer. Nat Rev Cancer 15, 96–109.

Bruhn S, Fang Y, Barrenas F, Gustafsson M, Zhang H, Konstantinell A, Kronke A, Sonnichsen B, Bresnick A, Dulyaninova N, et al. (2014). A generally applicable translational strategy identifies S100A4 as a candidate gene in allergy. Sci Transl Med 6, 218ra214.

Budayeva HG, Cristea IM (2016). Human Sirtuin 2 localization, transient interactions, and impact on the proteome point to its role in intracellular trafficking. Mol Cell Proteomics 15, 3107–3125.

Calle Y, Carragher NO, Thrasher AJ, Jones GE (2006). Inhibition of calpain stabilises podosomes and impairs dendritic cell motility. J Cell Sci 119, 2375–2385.

Chiaretti S, de Curtis I (2016). Role of liprins in the regulation of tumor cell motility and invasion. Curr Cancer Drug Targets 16, 238–248.

Clark K, Langeslag M, van Leeuwen B, Ran L, Ryazanov AG, Figdor CG, Moolenaar WH, Jalink K, van Leeuwen FN (2006). TRPM7, a novel regulator of actomyosin contractility and cell adhesion. EMBO J 25, 290–301.

Clark K, Middelbeek J, Lasonder E, Dulyaninova NG, Morrice NA, Ryazanov AG, Bresnick AR, Figdor CG, van Leeuwen FN (2008). TRPM7 regulates myosin IIA filament stability and protein localization by heavy chain phosphorylation. J Mol Biol 378, 790–803.

Collin O, Na S, Chowdhury F, Hong M, Shin ME, Wang F, Wang N (2008). Self-organized podosomes are dynamic mechanosensors. Curr Biol 18, 1288–1294.

Collin O, Tracqui P, Stephanou A, Usson Y, Clement-Lacroix J, Planus E (2006). Spatiotemporal dynamics of actin-rich adhesion microdomains: influence of substrate flexibility. J Cell Sci 119, 1914–1925.

Cougoule C, Le Cabec V, Poincloux R, Al Saati T, Mege JL, Tabouret G, Lowell CA, Laviolette-Malirat N, Maridonneau-Parini I (2010). Three-dimensional migration of macrophages requires Hck for podosome organization and extracellular matrix proteolysis. Blood 115, 1444–1452.

Cox S, Rosten E, Monypenny J, Jovanovic-Talisman T, Burnette DT, Lippincott-Schwartz J, Jones GE, Heintzmann R (2011). Bayesian localization microscopy reveals nanoscale podosome dynamics. Nat Methods 9, 195–200.

Deakin NO, Turner CE (2014). Paxillin inhibits HDAC6 to regulate microtubule acetylation, Golgi structure, and polarized migration. J Cell Biol 206, 395–413.

Destaing O, Saltel F, Gilquin B, Chabadel A, Khochbin S, Ory S, Jurdic P (2005). A novel Rho-mDia2-HDAC6 pathway controls podosome patterning through microtubule acetylation in osteoclasts. J Cell Sci 118, 2901–2911.

Donato R, Cannon BR, Sorci G, Riuzzi F, Hsu K, Weber DJ, Geczy CL (2013). Functions of S100 proteins. Curr Mol Med 13, 24–57.

Dong JM, Tay FP, Swa HL, Gunaratne J, Leung T, Burke B, Manser E (2016). Proximity biotinylation provides insight into the molecular composition of focal adhesions at the nanometer scale. Sci Signal 9, rs4.

Dulyaninova NG, Bresnick AR (2013). The heavy chain has its day: regulation of myosin-II assembly. Bioarchitecture 3, 77–85.

Erlandsson MC, Svensson MD, Jonsson IM, Bian L, Ambartsumian N, Andersson S, Peng Z, Vaaraniemi J, Ohlsson C, Andersson KM, Bokarewa MI (2013). Expression of metastasin S100A4 is essential for bone resorption and regulates osteoclast function. Biochim Biophys Acta 1833, 2653–2663.

Evans JG, Correia I, Krasavina O, Watson N, Matsudaira P (2003). Macrophage podosomes assemble at the leading lamella by growth and fragmentation. J Cell Biol 161, 697–705.

Evans JH, Falke JJ (2007). Ca^{2+} influx is an essential component of the positive-feedback loop that maintains leading-edge structure and activity in macrophages. Proc Natl Acad Sci USA 104, 16176–16181.

Fleetwood AJ, Achuthan A, Schultz H, Nansen A, Almholt K, Usher P, Hamilton JA (2014). Urokinase plasminogen activator is a central regulator of macrophage three-dimensional invasion, matrix degradation, and adhesion. J Immunol 192, 3540–3547.

Gil-Henn H, Destaing O, Sims NA, Aoki K, Alles N, Neff L, Sanjay A, Bruzzaniti A, De Camilli P, Baron R, Schlessinger J (2007). Defective microtubule-dependent podosome organization in osteoclasts leads to increased bone density in $Pyk2^{-/-}$ mice. J Cell Biol 178, 1053–1064.

Gimona M, Buccione R, Courtneidge SA, Linder S (2008). Assembly and biological role of podosomes and invadopodia. Curr Opin Cell Biol 20, 235–241.

Guiet R, Verollet C, Lamsoul I, Cougoule C, Poincloux R, Labrousse A, Calderwood DA, Glogauer M, Lutz PG, Maridonneau-Parini I (2012). Macrophage mesenchymal migration requires podosome stabilization by filamin A. J Biol Chem 287, 13051–13062.

Hanania R, Sun HS, Xu K, Pustylnik S, Jeganathan S, Harrison RE (2012). Classically activated macrophages use stable microtubules for matrix metalloproteinase-9 (MMP-9) secretion. J Biol Chem 287, 8468–8483.

Hashimoto D, Chow A, Noizat C, Teo P, Beasley MB, Leboeuf M, Becker CD, See P, Price J, Lucas D, et al. (2013). Tissue-resident macrophages self-maintain locally throughout adult life with minimal contribution from circulating monocytes. Immunity 38, 792–804.

Heizmann CW, Cox JA (1998). New perspectives on S100 proteins: a multifunctional Ca^{2+}-, Zn^{2+}- and Cu^{2+}-binding protein family. Biometals 11, 383–397.

Janke C, Bulinski JC (2011). Post-translational regulation of the microtubule cytoskeleton: mechanisms and functions. Nat Rev Mol Cell Biol 12, 773–786.

Kedziora KM, Leyton-Puig D, Argenzio E, Boumeester AJ, van Butselaar B, Yin T, Wu YI, van Leeuwen FN, Innocenti M, Jalink K, Moolenaar WH (2016). Rapid remodeling of invadosomes by Gi-coupled receptors: dissecting the role of Rho GTPases. J Biol Chem 291, 4323–4333.

Kiss B, Duelli A, Radnai L, Kekesi KA, Katona G, Nyitray L (2012). Crystal structure of the S100A4-nonmuscle myosin IIA tail fragment complex reveals an asymmetric target binding mechanism. Proc Natl Acad Sci USA 109, 6048–6053.

Kiss B, Kalmar L, Nyitray L, Pal G (2016). Structural determinants governing S100A4-induced isoform-selective disassembly of nonmuscle myosin II filaments. FEBS J 283, 2164–2180.

Kopp P, Lammers R, Aepfelbacher M, Woehlke G, Rudel T, Machuy N, Steffen W, Linder S (2006). The kinesin KIF1C and microtubule plus ends regulate podosome dynamics in macrophages. Mol Biol Cell 17, 2811–2823.

Kovacs M, Toth J, Hetenyi C, Malnasi-Csizmadia A, Sellers JR (2004). Mechanism of blebbistatin inhibition of myosin II. J Biol Chem 279, 35557–35563.

Kriajevska M, Fischer-Larsen M, Moertz E, Vorm O, Tulchinsky E, Grigorian M, Ambartsumian N, Lukanidin E (2002). Liprin beta 1, a member of the family of LAR transmembrane tyrosine phosphatase-interacting proteins, is a new target for the metastasis-associated protein S100A4 (Mts1). J Biol Chem 277, 5229–5235.

Labernadie A, Bouissou A, Delobelle P, Balor S, Voituriez R, Proag A, Fourquaux I, Thibault C, Vieu C, Poincloux R, et al. (2014). Protrusion force microscopy reveals oscillatory force generation and mechanosensing activity of human macrophage podosomes. Nat Commun 5, 5343.

Li ZH, Dulyaninova NG, House RP, Almo SC, Bresnick AR (2010). S100A4 regulates macrophage chemotaxis. Mol Biol Cell 21, 2598–2610.

Li ZH, Spektor A, Varlamova O, Bresnick AR (2003). Mts1 regulates the assembly of nonmuscle myosin-IIA. Biochemistry 42, 14258–14266.

Limouze J, Straight AF, Mitchison T, Sellers JR (2004). Specificity of blebbistatin, an inhibitor of myosin II. J Muscle Res Cell Motil 25, 337–341.

Linder S, Hufner K, Wintergerst U, Aepfelbacher M (2000). Microtubule-dependent formation of podosomal adhesion structures in primary human macrophages. J Cell Sci 113, 4165–4176.

Linder S, Wiesner C (2015). Tools of the trade: podosomes as multipurpose organelles of monocytic cells. Cell Mol Life Sci 72, 121–135.

Linder S, Wiesner C (2016). Feel the force: podosomes in mechanosensing. Exp Cell Res 343, 67–72.

Linder S, Wiesner C, Himmel M (2011). Degrading devices: invadosomes in proteolytic cell invasion. Annu Rev Cell Dev Biol 27, 185–211.

Marenholz I, Heizmann CW, Fritz G (2004). S100 proteins in mouse and man: from evolution to function and pathology (including an update of the nomenclature). Biochem Biophys Res Commun 322, 1111–1122.

Meddens MB, Pandzic E, Slotman JA, Guillet D, Joosten B, Mennens S, Paardekooper LM, Houtsmuller AB, van den Dries K, Wiseman PW, Cambi A (2016). Actomyosin-dependent dynamic spatial patterns of cytoskeletal components drive mesoscale podosome organization. Nat Commun 7, 13127.

Medina I, Cougoule C, Drechsler M, Bermudez B, Koenen RR, Sluimer J, Wolfs I, Doring Y, Herias V, Gijbels M, et al. (2015). Hck/Fgr kinase deficiency reduces plaque growth and stability by blunting monocyte recruitment and intraplaque motility. Circulation 132, 490–501.

Mitsuhashi M, Sakata H, Kinjo M, Yazawa M, Takahashi M (2011). Dynamic assembly properties of nonmuscle myosin II isoforms revealed by combination of fluorescence correlation spectroscopy and fluorescence cross-correlation spectroscopy. J Biochem 149, 253–263.

Miyauchi A, Hruska KA, Greenfield EM, Duncan R, Alvarez J, Barattolo R, Colucci S, Zambonin-Zallone A, Teitelbaum SL, Teti A (1990). Osteoclast cytosolic calcium, regulated by voltage-gated calcium channels and extracellular calcium, controls podosome assembly and bone resorption. J Cell Biol 111, 2543–2552.

North BJ, Marshall BL, Borra MT, Denu JM, Verdin E (2003). The human Sir2 ortholog, SIRT2, is an NAD+-dependent tubulin deacetylase. Mol Cell 11, 437–444.

Olson MW, Bernardo MM, Pietila M, Gervasi DC, Toth M, Kotra LP, Massova I, Mobashery S, Fridman R (2000). Characterization of the monomeric and dimeric forms of latent and active matrix metalloproteinase-9. Differential rates for activation by stromelysin 1. J Biol Chem 275, 2661–2668.

Sadoul K, Khochbin S (2016). The growing landscape of tubulin acetylation: lysine 40 and many more. Biochem J 473, 1859–1868.

Saleem M, Kweon MH, Johnson JJ, Adhami VM, Elcheva I, Khan N, Bin Hafeez B, Bhat KM, Sarfaraz S, Reagan-Shaw S, et al. (2006). S100A4 accelerates tumorigenesis and invasion of human prostate cancer through the transcriptional regulation of matrix metalloproteinase 9. Proc Natl Acad Sci USA 103, 14825–14830.

Santamaria-Kisiel L, Rintala-Dempsey AC, Shaw GS (2006). Calcium-dependent and -independent interactions of the S100 protein family. Biochem J 396, 201–214.

Schefe JH, Lehmann KE, Buschmann IR, Unger T, Funke-Kaiser H (2006). Quantitative real-time RT-PCR data analysis: current concepts and the novel "gene expression's CT difference" formula. J Mol Med (Berl) 84, 901–910.

Scheiter M, Lau U, van Ham M, Bulitta B, Grobe L, Garritsen H, Klawonn F, Konig S, Jansch L (2013). Proteome analysis of distinct developmental stages of human natural killer (NK) cells. Mol Cell Proteomics 12, 1099–1114.

Shi C, Pamer EG (2011). Monocyte recruitment during infection and inflammation. Nat Rev Immunol 11, 762–774.

Siddiqui TA, Lively S, Vincent C, Schlichter LC (2012). Regulation of podosome formation, microglial migration and invasion by Ca^{2+}-signaling molecules expressed in podosomes. J Neuroinflammation 9, 250.

Sun J, Lu F, He H, Shen J, Messina J, Mathew R, Wang D, Sarnaik AA, Chang WC, Kim M, et al. (2014). STIM1- and Orai1-mediated Ca^{2+} oscillation orchestrates invadopodium formation and melanoma invasion. J Cell Biol 207, 535–548.

Takenaga K, Nakamura Y, Sakiyama S (1994). Cellular localization of pEL98 protein, an S100-related calcium binding protein, in fibroblasts and its tissue distribution analyzed by monoclonal antibodies. Cell Struct Funct 19, 133–141.

Tauber S, Paulsen K, Wolf S, Synwoldt P, Pahl A, Schneider-Stock R, Ullrich O (2012). Regulation of MMP-9 by a WIN-binding site in the monocyte-macrophage system independent from cannabinoid receptors. PLoS One 7, e48272.

Tran AD, Marmo TP, Salam AA, Che S, Finkelstein E, Kabarriti R, Xenias HS, Mazitschek R, Hubbert C, Kawaguchi Y, et al. (2007). HDAC6 deacetylation of tubulin modulates dynamics of cellular adhesions. J Cell Sci 120, 1469–1479.

van den Dries K, Meddens MB, de Keijzer S, Shekhar S, Subramaniam V, Figdor CG, Cambi A (2013). Interplay between myosin IIA-mediated contractility and actin network integrity orchestrates podosome composition and oscillations. Nat Commun 4, 1412.

van der Vaart B, van Riel WE, Doodhi H, Kevenaar JT, Katrukha EA, Gumy L, Bouchet BP, Grigoriev I, Spangler SA, Yu KL, et al. (2013). CFEOM1-associated kinesin KIF21A is a cortical microtubule growth inhibitor. Dev Cell 27, 145–160.

Van Goethem E, Guiet R, Balor S, Charriere GM, Poincloux R, Labrousse A, Maridonneau-Parini I, Le Cabec V (2011). Macrophage podosomes go 3D. Eur J Cell Biol 90, 224–236.

van Helden SF, Oud MM, Joosten B, Peterse N, Figdor CG, van Leeuwen FN (2008). PGE2-mediated podosome loss in dendritic cells is dependent on actomyosin contraction downstream of the RhoA-Rho-kinase axis. J Cell Sci 121, 1096–1106.

Visser D, Langeslag M, Kedziora KM, Klarenbeek J, Kamermans A, Horgen FD, Fleig A, van Leeuwen FN, Jalink K (2013). TRPM7 triggers Ca2+ sparks and invadosome formation in neuroblastoma cells. Cell Calcium 54, 404–415.

Weatherly K, Bettonville M, Torres D, Kohler A, Goriely S, Braun MY (2015). Functional profile of S100A4-deficient T cells. Immun Inflamm Dis 3, 431–444.

Wiesner C, Faix J, Himmel M, Bentzien F, Linder S (2010). KIF5B and KIF3A/KIF3B kinesins drive MT1-MMP surface exposure, CD44 shedding, and extracellular matrix degradation in primary macrophages. Blood 116, 1559–1569.

Zhang G, Li M, Jin J, Bai Y, Yang C (2011). Knockdown of S100A4 decreases tumorigenesis and metastasis in osteosarcoma cells by repression of matrix metalloproteinase-9. Asian Pac J Cancer Prev 12, 2075–2080.